

Shaped pupil coronagraph design improvements for the WFIRST Coronagraph Instrument

A J Eldorado Riggs^a, Neil T. Zimmerman^b, Bijan Nemati^c, John Krist^a

^aJet Propulsion Laboratory, California Institute of Technology, Pasadena, CA 91109

^bNASA Goddard Space Flight Center, Greenbelt, MD 20771

^cUniversity of Alabama in Huntsville, Huntsville, AL 35899

ABSTRACT

NASA’s WFIRST Coronagraph Instrument (CGI) is planned to image and characterize exoplanets at high contrast. The CGI operating modes are the hybrid Lyot coronagraph for planet detection and inner debris disk imaging, a shaped pupil coronagraph for planet characterization, and another shaped pupil for outer disk imaging. Early CGI designs focused on overcoming the diffraction of the large pupil obscurations. Now that those designs have been proven to work in the lab, the design emphasis has been on achieving higher throughput and lower sensitivities to jitter and polarization aberrations. Here we present those improvements and the integration of science yield modeling into the spectrographic shaped pupil design process.

Keywords: WFIRST, CGI, coronagraph, exoplanet

1. INTRODUCTION

The Wide-Field Infrared Survey Telescope (WFIRST) is a 2.4-meter flagship observatory planned to launch in 2026.¹ It was the top-ranked mission in the 2010 Decadal Survey of Astronomy and Astrophysics entitled New Worlds, New Horizons.² The Wide-Field Instrument (WFI) will perform a dark energy survey and a census of exoplanets via gravitational microlensing. A secondary instrument, the Coronagraph Instrument (CGI), will study cool exoplanets and circumstellar debris disks around nearby stars. The main goals of the CGI are to image and spectrally characterize several cool gas giant exoplanets, to image exozodiacal dust for the first time in visible light, and to demonstrate high star-to-planet contrast coronagraphs and wavefront correction for a future exo-earth characterizing mission in space.

The CGI will have two types of coronagraphs operating in three modes. The hybrid Lyot coronagraph (HLC) uses large static deformable mirror (DM) shapes, a phase- and amplitude- controlling focal plane mask (FPM), and Lyot stop (LS) to suppress starlight.³ The HLC will primarily be used in a $\Delta\lambda/\lambda_c = 10\%$ bandpass at 575 nm for exoplanet detection and inner debris disk imaging in a 360° field of view from $3 - 9 \lambda_c/D$ (150-450 milliarcseconds at 575 nm), where λ_c is the central wavelength of the bandpass and D is the diameter of the telescope. The other two modes use shaped pupil Lyot coronagraphs (SPLCs), which suppress starlight with a binary-amplitude shaped pupil apodizer, a binary-amplitude FPM with an outer diaphragm, and a Lyot stop.⁴ Spectroscopy will be performed with an integral field spectrograph (IFS) mainly in 18% spectral bandwidths at 660 nm and 770nm. The SPLC-IFS design has an azimuthally restricted field of view in two mirrored 65° annular sectors from $2.6 - 9 \lambda_c/D$. Three orientations of the SPLC-IFS masks are included at each bandpass to allow a full field of view. The other SPLC has a full 360° field of view from $6.5 - 20 \lambda_c/D$ (set by the controllable Nyquist limit of the DMs) for outer debris disk imaging. The SPLC-disk design will mostly be used in the 10% bandpass at 575nm.

Coronagraph design and verification for the WFIRST observatory have been challenging but steadily improving. The first major obstacle was overcoming the extra diffraction from the pupil obscurations shown in Figure 1: a large secondary mirror ($\approx 31\%$ D in diameter) and six thick, non-radial struts (2.6% D wide).

Send correspondence to A.J. Riggs: aj.riggs@jpl.nasa.gov

©2017 California Institute of Technology. Government sponsorship acknowledged.

Coronagraphs perform better for open apertures; pupil obscurations make it more difficult for a coronagraph to suppress starlight without also suppressing off-axis light (from exoplanets and disks) and increase coronagraphs' sensitivities to jitter. Because WFIRST CGI is a real upcoming mission, we must also consider manufacturability and alignment tolerances. For the first three years of WFIRST coronagraph development, the main goals were to invent,^{3–5} manufacture,^{6,7} and lab test^{8–11} the coronagraphs. Since then accurate and precise Fresnel-based optical modeling to predict testbed and CGI performance has also become a priority.^{12–16} In the past year, the primary goals of the coronagraph design have been 1) to increase the low off-axis throughput for the two validated architectures (HLC and SPLC) and 2) to improve the robustness to wavefront disturbances and mask misalignments.

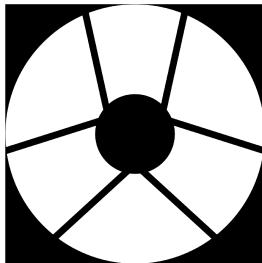


Figure 1. The WFIRST pupil.

In this paper, we detail our efforts in the past year to improve the SPLC optimization for the WFIRST CGI. The last major development for the SPLC was its invention in 2014,^{4,5} when a FPM and Lyot stop were added to the optimization of the apodizer-only shaped pupil coronagraph (SPC).^{17–19} (The reader should note that most documents about the WFIRST CGI refer to the SPLC as an SPC. This is because the SPC was initially selected for WFIRST, but all designs since autumn of 2014 have been SPLCs. Any uses of SPC hereafter in this text also refer to SPLCs.) Section 2 explains how we increase misalignment and rollover tolerances by padding the nominal obscurations underlying the shaped pupil mask. In Section 3, we describe several improvements to the optimization process itself to improve speed, numerical stability, and usefulness of the output. Sections 4 and 5 detail our modest improvements to the design process, performance, and robustness of the SPLC-IFS and SPLC-disk modes, respectively. Finally, Section 6 describes several investigations into slightly different coronagraph architectures, such as the apodized pupil Lyot coronagraph (APLC), that might provide higher performance than the baselined SPLCs.

2. PRIMARY MIRROR ROLLOVER

Before optimizing a shaped pupil, we pad all the obscurations of the underlying input pupil to allow for small misalignment or magnification errors between the telescope and instrument. For the past two years, we have padded the pupil all the flight design shaped pupils by 0.2% of the telescope diameter, D , normal to each edge. Thus, the struts become 0.4% D thicker than their nominal width of 2.6% D , the outer diameter shrinks by 0.4% D , and the inner diameter grows by 0.4% D from the nominal value of 30.1% D . The 0.2% padding is the minimum expected amount for acceptable CGI and WFIRST pupil alignment. More padding would ease alignment tolerances but would significantly reduce throughput. All uses of the terms throughput or core throughput in this paper refer to the maximum summed intensity within the half-max of the main lobe of off-axis point-spread function (PSF) divided by the total intensity incident upon the primary mirror. We ignore reflectivity and absorption losses from optical surfaces in the core throughput calculation when optimizing the coronagraph design because most of the optical surface losses would be common to any coronagraph type.

We recently discovered that the shaped pupil designs require even more padding of the outer diameter. The measured map of the primary mirror, which cannot be shown due to export regulations and proprietary regulations, contains a large lip or rollover along the outer edge. Krist et al.¹³ found that the previous shaped pupil coronagraph designs, which have narrow openings along the outer edge, cannot achieve better than approximately 10^{-7} raw contrast with the rollover present. In the newest SPLC designs reported in Sections 4 and 5

in this paper, we padded the input pupil’s outer diameter by an extra 0.5% on each side, which is another 1.0% in total. This extra padding degrades the core throughput of the IFS-mode shaped pupil coronagraph designs (when no other changes are made) by a factor of 0.8 to 0.9. Fortunately, we show strategies in Sections 4 and 5 that more than offset for the core throughput loss from blocking the primary mirror rollover.

3. GENERAL IMPROVEMENTS TO THE SPLC OPTIMIZATION

Over the past few months, we have made several improvements to the original SPLC optimization method described in Zimmerman et al.⁴ In this section, we present upgrades to the optimization itself in the areas of speed, numerical stability, and usability of the output.

3.1 Monochromatic First Propagation in a Broadband Optimization

The most computationally expensive matrix Fourier transform (MFT) in an SPLC optimization is from the apodizer plane to the first focal plane. Soummer et al.²⁰ and Vanderbei¹⁹ describe the MFT and the cases for which it is faster than a conventional fast Fourier transform (FFT). In the original SPLC optimization code described by Zimmerman et al.,⁴ broadband optimizations propagated through the whole coronagraph at each sampled wavelength over the desired bandpass. This approach is relatively straightforward to program and requires just one representation of each mask to be used for all the wavelengths. We recently recalled that the electric field at the focus immediately after the apodizer is the same at every wavelength (except for scaling radially), so the MFT from the apodizer to the first focal plane can be performed at just one wavelength. (This assumes a flat wavefront entering the coronagraph and an amplitude-only apodizer.) The FPM then needs to be defined separately at each wavelength. This monochromatic first propagation approach can increase the SPLC optimization speed by several times in some cases, especially with higher numbers of points in the apodizer and/or the FPM.

This approach can also be used in the broadband, 2-D optimization of apodized pupil Lyot coronagraphs (APLCs),^{4,21} which use Babinet’s principle to compute the Lyot plane electric field.²⁰ The original APLC code with a broadband first propagation could only use the interior point method, which can utilize multiple cores to complete in minutes to hours. The interior point method in this case requires tens to hundreds of gigabytes of RAM for broadband, high-resolution optimizations. When written with the monochromatic first propagation, there is a trade of time for RAM. In this case, the APLC optimization can only run with the dual simplex method on a single core and thus takes several days, but only a few gigabytes of RAM are necessary. We are still investigating why the interior point method no longer converges for this different propagation strategy. In summary, it is usually beneficial to use the monochromatic first MFT for any SPLC optimization, but it is only a good idea for APLC optimizations when there is not enough RAM available for the other method.

3.2 Re-scaling Variables

Optimizations can encounter numerical trouble when the scales of different variables are several orders of magnitude apart. This occurs in the linear SPLC optimization when the DFTs are written directly as the physical propagation equations. When designing an SPLC for high contrast, the stellar electric field decreases by two or more orders of magnitude as it passes through each the focal plane mask and then the Lyot stop. It is therefore beneficial for the linear program to insert a scaling factor of approximately 10^2 (a good value for a given case should be found empirically and needs only coarse tuning) in each of the 2-D MFTs from the apodizer to the FPM and from the FPM to the Lyot stop. These extra scaling factors must also be accounted for in the contrast constraint equations.

Prior to including the scaling factors, the linear SPLC optimization code could only be performed with the dual simplex method. With the scaling factor, the linear SPLC optimization can now also be performed with the interior point method, which can sometimes be much faster at the expense of using more RAM and multiple cores. The scaling factor also reduced SPLC convergence time when using the dual simplex method.

3.3 Minimally Sized Planes

One straightforward and simple strategy to reduce optimization time is to compute the electric field only where it is used. Because we must use two 1-D discrete Fourier transforms (DFTs) in series to perform a 2-D DFT as explained by Vanderbei,¹⁹ this means calculating the field in the smallest rectangle encompassing the desired region. For simplicity when testing new code or running a one-off optimization, it is easier to define coordinates on square arrays and to define the Lyot stop out to the full pupil diameter. Large design surveys can sometimes be performed several times faster, however, if the focal planes are cropped down to rectangles encompassing only the FPM opening or search area (when the field of view is not a full 360°) and the Lyot plane is cropped down to the size of the Lyot stop opening.

3.4 Pixel-Centered Shaped Pupil for FFT-based Analysis

As described by Vanderbei,¹⁹ exploiting symmetry is a key factor in making shaped pupil optimizations fast and tractable. Symmetry of the apodizer about the x- or y-axis simplifies the complex-valued MFT along that line of symmetry into a real-valued sum in just half the plane. Previously, we had always centered the shaped pupil in between pixels to write the MFT more simply. As an illustrative example in 1-D, the MFT with symmetry in x from the discretized apodizer $A(x_k)$ to the discretized focal plane electric field $E_f(\xi_j)$ is

$$\begin{aligned} \Delta x &= D/N_x, & N_x \text{ is even,} & & x_k &\in ([1, 2, \dots, N_x] - 1/2) \cdot \Delta x, \\ E_f(\xi_j) &= 2 \sum_{k=1}^{N_x} A(x_k) \cos(2\pi x_k \xi_j) \Delta x, & j &\in [1, 2, \dots, N_\xi], \end{aligned} \quad (1)$$

when the apodizer is inter-pixel centered with an even number of points N_x across half the pupil diameter D and an even number of points N_ξ across the relevant half of the focal plane.

Nearly all Fresnel-based propagation packages such as PROPER²² utilize FFTs, which expect the pupil to be centered on a pixel. Without manual intervention in an FFT-based propagation code, the inter-pixel centering of the apodizer causes the pupil to shear one pixel along each axis at each consecutive pupil plane. This effect is undesirable and tedious to counteract, so we have shifted the coordinates of the apodizer by half a pixel to have an odd number of points and be pixel centered. The MFT therefore needs an extra term,

$$\begin{aligned} \Delta x &= D/(N_x - 1), & N_x \text{ is odd,} & & x_k &\in [0, 1, \dots, (N_x - 1)] \cdot \Delta x, \\ E_f(\xi_j) &= A(0)\Delta x + 2 \sum_{k=1}^{N_x} A(x_k) \cos(2\pi x_k \xi_j) \Delta x, & j &\in [1, 2, \dots, N_\xi], \end{aligned} \quad (2)$$

in order not to double count the values along the axis of symmetry. The apodizer solution, once filled in by mirroring about the x-axis, will have an odd number of points in the full plane and needs to be unevenly zero-padded to obtain the pixel-centered pupil and even-sized array desired for an FFT. It is straightforward to extend Equation 2 to a 2-D MFT with one or two axes of pupil symmetry.

4. IMPROVEMENTS TO THE SPC-IFS DESIGN

Prior to this year, the last major design improvement for the general category of shaped pupil coronagraphs was the inclusion of a Lyot stop in the optimization.^{4,5} The SPLC provides higher contrast at a smaller inner working angle (IWA) than an apodizer-only shaped pupil coronagraph. The IWA is defined as the angular separation from the star at which the core throughput of an off-axis point source is half of its maximum value within the dark hole; the outer working angle (OWA) is defined similarly except it is at the farther angular separation. The first SPLCs had an annular Lyot stop in keeping with prior Lyot coronagraph conventions, but we recently discovered that different Lyot stop shapes can provide higher throughput in some cases. In parallel, we discovered that the tip/tilt (T/T) sensitivities of SPLC designs varied unpredictably by factors of a few when the other design parameters were changed. After including the new Lyot stop shape and T/T insensitivity into the optimization code, there were too many possible combinations of raw contrast, throughput, and IWA to choose from by intuition. Because our end goal is to maximize the number of exoplanet spectra obtained, we developed a design pipeline to model the performance and science yield for each SPLC design in a given survey.

4.1 Better Choice of Lyot Stop Shape

To obtain the best performance when designing a coronagraph, it is important to consider simultaneously the suppression of the on-axis starlight and transmission of the off-axis planet and disk light. Figure 2(a) shows both for the 2015-2016 WFIRST CGI SPC-IFS design (re-computed to block the primary mirror rollover). Until this year we had not considered the shape of the transmitted off-axis light at the Lyot plane compared to the Lyot stop. From Figure 2(a), it is clear that the annular Lyot stop is not a good match. After the shaped pupil mask gets low-pass filtered through the FPM, there is essentially no off-axis light along the horizontal axis of the Lyot plane. The Lyot stop therefore only needs to be open in the two main regions illuminated by off-axis sources.

As a first attempt at a new Lyot stop shape, we blocked part of the annulus by the same amount as the bowtie FPM is open, 65° , as shown in Figure 2(b). In this new design (referred to as SPC 20170714) optimized for the new Lyot stop, almost none of the off-axis light from the science target is lost in the newly blocked region of the Lyot stop. In fact, the throughput increased from 3.00% to 3.85% because the shaped pupil did not have to work as hard and thus had a higher transmission. The shaped pupil and FPM instead diffract more of the starlight behind the newly blocked parts of the Lyot stop. In the near future we will investigate more optimal Lyot stop shapes, but while we improve other parts of the optimization it is simpler to have only the three wedge parameters (inner diameter, outer diameter, and opening angle) to vary in design surveys.

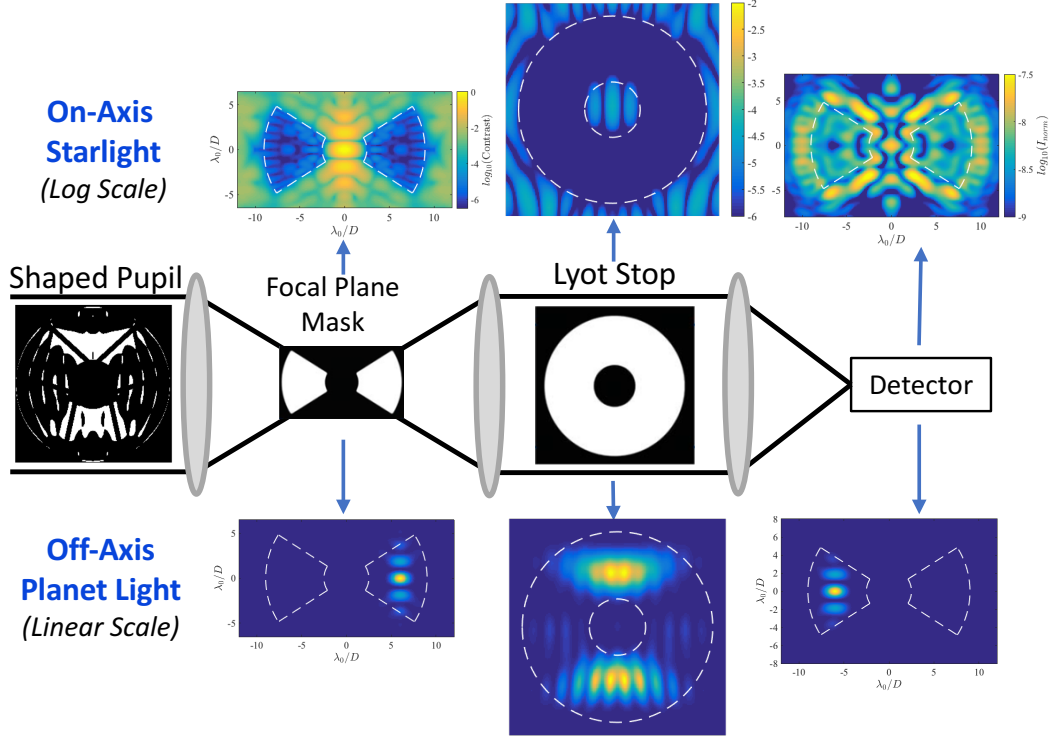
For reference, here we enumerate the parameters of the SPC 20170714 design. The shaped pupil is optimized on a 1000×1000 array, and its values are rounded to have binary amplitudes. The padding of the input pupil is described in Section 2. The bowtie FPM is open from $2.6 - 9.0\lambda_c/D$ in two symmetric 65° annular segments, and the dark hole region has the same footprint in the final focal plane. The Lyot stop is open from 25%-82% of the diameter in symmetric 115° annular segments. The design has a core throughput of 3.85% and an ideal raw contrast of approximately 2×10^{-9} .

The new bowtie or wedge-shaped Lyot stop does not always yield higher throughput for an SPLC. One example is when there is a 360° dark hole. The apodization is then more evenly distributed over the whole aperture, so the Lyot plane is still illuminated at most angles. Figure 3 shows a second case that applies to the $2 \times 65^\circ$ dark holes. The raw contrast constraint was varied for each the 2015-2016 annular Lyot stop SPLC and the 20170714 design with the bowtie Lyot stop, and all other parameters were held constant. The wedge Lyot stop only yields higher core throughput at higher contrasts such as the current operating point. The core throughput is the same for both Lyot stops between 10^{-8} and 10^{-7} raw contrast. Above 10^{-7} contrast, the annular Lyot stop yields higher throughput because the shaped pupil is no longer mostly blacked out along the horizontal axis. The smaller Lyot stop opening of the wedge Lyot stop lowers the maximum throughput at low to moderate contrasts when the shaped pupil is less obscured. This comparison may become relevant if the SPLC raw contrast is ever relaxed and then recovered with some other method, such as with the DMs, to increase throughput.

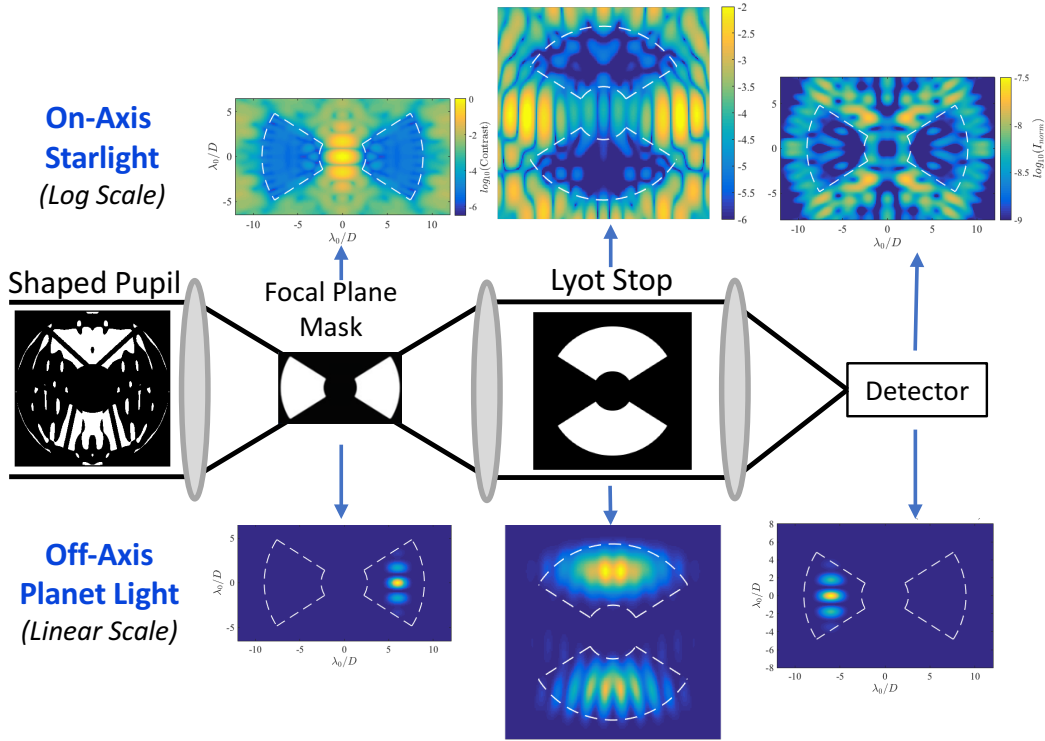
4.2 Reduced Low-Order Aberration Sensitivities

To guarantee sufficient T/T insensitivity during design surveys, we investigated several methods of enforcing it in the SPLC optimization. We first tested the indirect method developed by N'diaye et al.²³ for APLCs of extending the dark hole behind the edges of the FPM by some amount. It is unclear why this approach works for the APLC because the constraint is being applied on the final focal plane, whereas the relevant interaction occurs at the plane of the FPM. This method produced pseudo-random results for SPLC optimizations, so the T/T sensitivity still varied by factors of up to 4 between designs with only a small change to any given design parameter.

After postulating that the T/T sensitivity depended on the speckle pattern along the bowtie FPM's edge, we tested a second indirect method that uniformly suppressed the speckles in the first focal plane on both sides of the FPM's edges. This extra constraint was performed at high resolution (≈ 60 pixels per λ_c/D because 1 mas at 660nm is $\approx 1/56 \lambda_c/D$). A contrast constraint of $\approx 10^{-4}$ and a ± 2 mas suppression band improved the T/T sensitivity by several times for up to 1 mas RMS of pointing jitter, but the core throughput decreased drastically by a factor of 2-3. This method sacrificed too much throughput to use but proved that T/T sensitivity could be improved by trading core throughput.



(a) Previous SPC-IFS Design from 2015-2016 (Updated for Primary Mirror Rollover): 3.00% Core Throughput



(b) New SPC-IFS Design (SPC 20170714): 3.85% Core Throughput

Figure 2. Diagrams of the on-axis and off-axis intensities at each pupil and focal plane for (a) the previous SPC-IFS design updated to block the rollover on the primary mirror and (b) the most recent SPC-IFS design. The Lyot stop of the newer design more closely matches the shape of the off-axis light and blocks more on-axis light, thereby providing higher contrast and higher throughput. White dashed lines on the intensity maps indicate the mask edges.

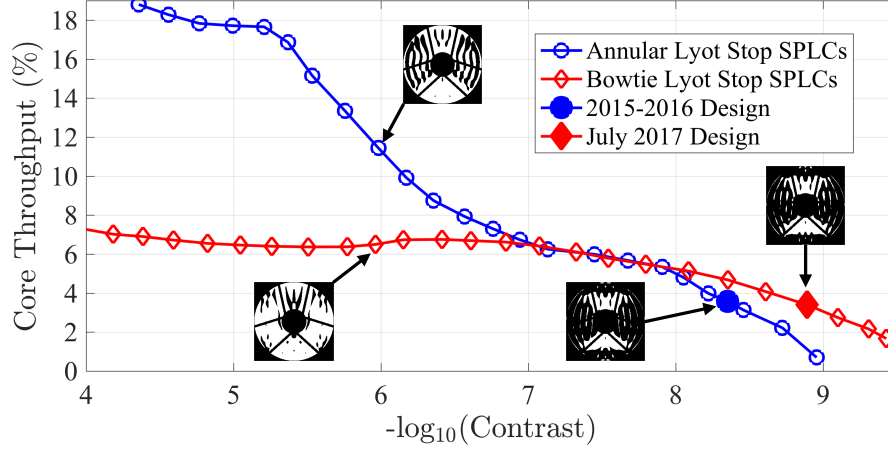


Figure 3. Comparison of core throughput vs average raw contrast in the dark hole for the SPLC-IFS with either an annular or $2 \times 115^\circ$ bowtie Lyot stop. All other parameters were held constant, and the pupil rollover was not blocked for this set of designs. The bowtie Lyot stop only provides better throughput for raw contrasts below $\approx 10^{-8}$. Above $\approx 10^{-7}$ raw contrast, the annular Lyot stop gives more throughput because the shaped pupil no longer blocks all the light along the horizontal axis of the pupil. The shaped pupil masks are shown for four points.

We postulated that the most efficient trade of these two parameters would come from a direct optimization. We had initially avoided direct optimization for T/T because it requires breaking the symmetries that make the MFT calculations so efficient. In fact, we implemented many of the speed improvements detailed in Section 3 to perform design surveys with the direct T/T constraints in a reasonable amount of time. Similar to why it was redundant to compute the electric field incident upon the first focal plane at each wavelength (as explained in Section 3.1), it would be wasteful to compute the Fourier-shifted electric field again for tipped or tilted input wavefronts. Instead, we kept the same on-axis electric field and included \pm translated versions of the FPM at the middle and two end wavelengths of the bandpass. In the case of the WFIRST CGI, the electric field is then needed in a half plane for the tipped or tilted wavefront instead of just the quadrant used for the on-axis propagation. As described in Appendix A2 of Zimmerman et al.,⁴ the enforced symmetry across the y-axis of the WFIRST pupil (as oriented in the figures of this paper) creates symmetry in the focal plane electric field: the real part is symmetric about both axes, and the imaginary part is symmetric about the y-axis and antisymmetric about the x-axis. These symmetries enable the electric field in the half plane to be obtained from the single quadrant already being computed.

We included tip (i.e., vertical FPM translation translations) in the optimization first to verify functionality but have not yet included tilt (i.e., horizontal FPM translations). This strategy nevertheless produced desirable T/T insensitivity. Figure 4 shows the trade of throughput and raw contrast for different amounts of RMS pointing jitter. Although the optimizations use only two vertical offsets of the FPM, for evaluation we use 29 points with Gaussian rolloff out to a radius of three times the RMS value. The highest throughput design has no T/T constraints in its optimization and thus suffers worse contrast degradation for increasing amounts of T/T. The WFIRST CGI is expected to have 0.4-1.6 mas of residual RMS pointing jitter. Adding any tip constraints into the optimization decreases the throughput but greatly improves the T/T insensitivity. The curves for decreasing amounts of throughput correspond to increasing resistance to T/T. Attempting to improve the T/T sensitivity even more with larger tip offsets in the optimization was ineffective and only decreased throughput. Design SPC 20170714 was optimized with this tip-only constraint method and corresponds to the second darkest curve on the plot.

Directly optimizing for T/T had the unintended but desirable effect of reducing sensitivities to other low-order Zernike aberrations as well. Figure 5 shows the RMS radial raw contrast change from 100 picometers RMS of several Zernike modes for (a) the ideal 2015-2016 SPLC-IFS design and (b) the ideal SPC 20170714 design. Krist et al.¹³ obtain similar sensitivity curves for SPC 20170714 after simulating optical aberrations and

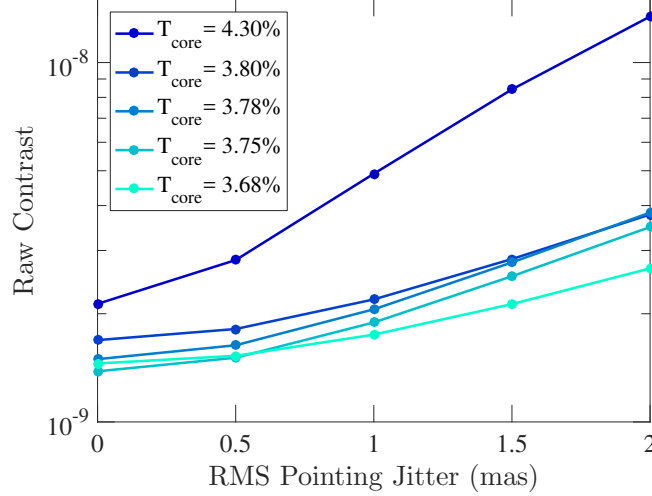


Figure 4. SPC-IFS raw contrast dependence on RMS tip/tilt jitter and core throughput. The highest throughput design was not optimized for any robustness to tip/tilt. Adding any jitter robustness causes a sizable drop in throughput but greatly improves raw contrast in the presence of jitter. The different curves are for designs with linearly increasing amounts of vertical offsets (according to the orientation in Figure 2) included at the focal plane mask in the optimization.

wavefront aberrations. These improved sensitivities make the new SPLC designs robust against the expected levels of WFIRST telescope wavefront jitter that will be too fast for the low-order wavefront sensing and control loop to correct. The new design is also less sensitive to the large amounts of astigmatism (e.g., ≈ 1 nm RMS at 770nm) and T/T from WFIRST primary mirror polarization aberrations. These results are also modeled by Krist et al.¹³

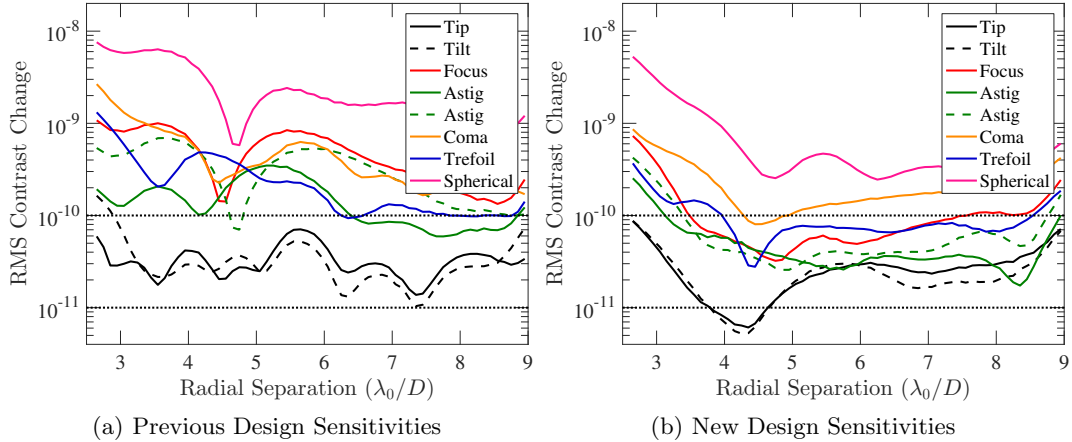


Figure 5. Comparison of SPC-IFS design sensitivities to 100 picometers RMS of Zernike aberrations for (a) the previous, 2015-2016 design and (b) the most recent point design, SPC 20170714. Optimizing for reduced tip/tilt sensitivity also improved sensitivities to other low-order modes.

4.3 SPC-IFS Design Pipeline for the WFIRST CGI

The SPC-IFS design improvements detailed in Sections 4.1 and 4.2 have opened a vast, continuous parameter space of feasible solutions. To obtain the optimal set of parameters, we first need to choose a cost function and constraints. The logical cost function to maximize is the science yield: the number of RV-detected exoplanet spectra at the desired SNR in the total allotted time. A direct, nonlinear optimization of SPLC masks for the science yield is intractable, so we have compartmentalized the optimization into a multi-step design pipeline.

The first step utilizes the same optimization code we have already been using. The SPLC optimization has millions of variables, so it needs to stay a linear (or quadratic and convex) program to be tractable. Each SPLC optimization for the IFS can be run in a few minutes, so it is feasible to perform a grid search over the input design parameters (e.g., IWA, OWA, Lyot stop shape, raw contrast, T/T insensitivity, and spectral bandwidth) for hundreds or thousands of configurations. We use the AMPL programming language and Gurobi solver, and we use a Python wrapper to generate AMPL programs with different input parameters and then run those jobs in parallel.

The second step of the design pipeline computes the engineering performance data (e.g., raw contrast, core throughput, and PSF core area all as functions of separation from the star) for each set of masks from the first step. The three most important effects to model are T/T from pointing jitter and finite stellar size, polarization aberrations from the primary mirror, and misalignments of the masks and DMs unknown to the estimation and control model. Closed-loop estimation and control simulations are necessary to determine the recoverable contrast in the presence of the polarization aberrations and unknown misalignments. As demonstrated by Zhou et al.¹⁴ and Marx et al.,¹⁵ we must use the Monte Carlo method for modeling the misalignments because we know only the uncertainty of our calibration measurements. We have not yet included the Monte Carlo misalignments in the design pipeline, but we have incorporated the polarization and T/T aberrations. Because the pointing jitter requires thousands of tipped/tilted wavefronts (for each wavelength and each of the four polarization states) to be propagated through the entire coronagraph model, we only compute the PSF with tip/tilt after the closed-loop correction has completed. It remains to be verified that pointing jitter and finite stellar size do not degrade the speed or achievable contrast of coronagraphic wavefront correction. By using an efficient control Jacobian calculation as mentioned by Krist et al.¹³ and a simplified model of the CGI, we can run a closed-loop, minimalistic wavefront correction simulation in approximately 20 minutes on our server. With ten Monte Carlo runs per design, this step will take approximately three hours and be the bottleneck in the pipeline.

The third step of the pipeline uses the engineering performance data to compute the number of obtained RV-detected exoplanet spectra. We use a Matlab function developed and described by Nemati et al.²⁴ for the yield calculations. The function is an exposure time calculator based on the coronagraph performance, estimated properties of the RV-detected exoplanets, estimated detector noise, estimated post-processing gain factor in raw contrast, and chosen quantities (e.g., desired SNR and maximum exposure time per target). This calculator takes only a fraction of a second per evaluation.

The fourth and final step is to evaluate the number of exoplanet spectra and their integration times from step 3. We can then decide whether to modify the grid search parameters and/or the constraints in step 1 to boost the yield further based on any apparent trends. The yield of spectra does not vary smoothly or monotonically for many variables because there is a discrete set of exoplanets to work with. For instance, increasing the IWA blocks closer-in exoplanets but makes some larger separation exoplanets characterizable because the core throughput increases.

Because there is some uncertainty for the amount of pointing jitter and much uncertainty for the albedo and size (and therefore the flux) of the exoplanets, our final design choice should provide the best averaged performance for the ranges of possible parameters. Our upcoming work on the pipeline will focus on developing this statistical selection of the best coronagraph design. We will need to choose the ranges and profiles (e.g., uniform or Gaussian) for the uncertain parameters as well as how best to average the results. We will then want to choose a design with an adequate average number of spectra and a small standard deviation in order to be robust against the astrophysical and engineering uncertainties.

5. IMPROVEMENTS TO THE SPC-DISK DESIGN

The WFIRST CGI SPLC debris disk imaging mode has received less attention than the other two modes because of its much larger inner working angle, which prevents it from seeing many, if any, exoplanets. It is nevertheless the only CGI mode capable of imaging debris disks at high contrast at separations out to $20\lambda_c/D$ (1.0 arcsec at 575nm), so it might be widely used during the allocated guest-observer time. The large IWA makes the SPLC-disk mode essentially immune to any likely levels of T/T and other low-order Zernike aberrations from pointing jitter, thermal jitter, and polarization aberrations. In this section, we present two types of improvements

to the SPLC-disk design. Higher resolution of the shaped pupil mask improves the achievable contrast, and a new objective function (also called a cost function) in the optimization enables a higher core throughput and a smaller IWA.

5.1 Higher Resolution

The shaped pupil mask optimizations usually produce nearly binary designs. Because we can manufacture only binary amplitudes, we round the shaped pupil solution. If the mask sampling is sufficiently high, then the degradation in raw contrast can be negligible when rounding the non-binary solution. In 2015 we had concluded that 1000×1000 resolution of the shaped pupil's binary array was sufficient for the SPLC disk science design. In Figure 6B from Zimmerman et al.,²⁵ there is still a contrast degradation of 1.5-2 times for that sampling. For the disk science design currently in the testbed, SPC 20170130b, we optimized for the highest allowable contrast and were able to obtain 9×10^{-10} raw contrast with 5.55% core throughput compared to the 2015-2016 design with 3.0×10^{-9} raw contrast and 5.65% core throughput. (Those throughput values were without primary mirror rollover blocking.) When the new design is rounded at 1000×1000 sampling the contrast degrades to 1.8×10^{-9} , but when rounded at 2000×2000 sampling the contrast stays at the design level of 9×10^{-10} . We therefore manufactured the SPC 20170130b design at the higher resolution for the Hight Contrast Imaging Testbed (HCIT) tests currently underway at the Jet Propulsion Laboratory.

The manufacturing of the disk science mask design is described by Balasubramanian et al.⁷ Two variations of this shaped pupil mask were manufactured, SPC 20170130a and SPC 20170130b. They were each 23.15mm in diameter with a 3mm wide black silicon outer ring to absorb stray light. The shaped pupil mask designs were made $1/\cos(8^\circ)$ times longer in the horizontal direction to account for the projection from the 8° angle of incidence. The SPC 20170130a design was optimized on a 1000×1000 grid and the amplitude was rounded to the nearest $1/4$. The non-binary pixels were up-sampled into 2×2 grids and made binary to have the equivalent total amplitude (e.g., a pixel with 75% amplitude at the original resolution as converted into three smaller pixels with zero transmission and one with full transmission). This partial up-sampling strategy also does not suffer from any degradation in raw contrast. By chance, the manufactured shaped pupil with the fewest number of defects was of the SPC 20170130b design, so it was the one chosen for use in the HCIT. Balasubramanian et al.⁷ show that the few defects on that shaped pupil have a negligible impact on expected performance. The transmissive annular FPMs are made of metal on anti-reflection coated glass. The openings are from $6.5 - 20\lambda_c/D$ at the intended disk science bandpasses of 565nm and 721nm, and they have a stretch of $1/\cos(3.5^\circ)$ to account for a 3.5° angle of incidence. (The 565nm band for the CGI has since changed to 575nm.) The through-hole, etched silicon Lyot stop with an annular opening from 26-88% of the pupil diameter and two thin support struts was re-used from a prior HCIT configuration for the SPLC-IFS.

5.2 New Objective Function

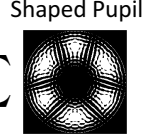
The major improvement to the SPLC-disk design is a new choice of objective function in the optimization. In the original shaped pupil optimizations,^{5,18,19} the objective function maximized was the transmission of the shaped pupil apodizer as shown in Figure 6. For pupils with at least one Cartesian axis of symmetry, this is equivalent to maximizing the peak, real electric field value at the first focal plane after the apodizer. (The realness assumes that the $1/\sqrt{-1}$ term is omitted from the optical Fourier transform for easier bookkeeping of complex terms.) For simplicity, when we first developed the SPLC, we used the same cost function.⁴

Ideally we would maximize the amount of useful off-axis light in the final focal plane, which is the core throughput. It is currently too difficult to maximize this sum of intensities within a variable-sized area. We have nevertheless moved closer to that goal by changing the objective function from the peak value in the first focal plane to the peak off-axis electric field value in the post-coronagraphic focal plane. Figure 6 shows how the previous and new cost functions are computed. For the new cost function, we approximate the off-axis SPLC propagation as on-axis propagation from the shaped pupil mask through a circular pinhole and then through the Lyot stop. The logical choice of pinhole diameter is approximately the width of the SPLC's FPM opening. Using a circular pinhole instead of the translated focal plane mask once again enables us to exploit symmetry to reduce the number of computations in the multi-plane, complex electric field propagation.

Old Cost Function:

= SP transmission
 = peak at 1st focus

$$\max \sum_x \sum_y$$

**New Cost Function:**

= spatially filtered SP x LS transmission
 \approx off-axis peak at post-coronagraphic focus

$$\max \sum_x \sum_y$$

Spatially filtered SP
 within LS opening

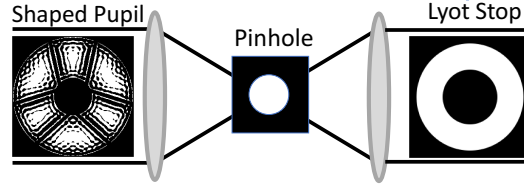
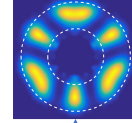


Figure 6. The new and old cost functions being maximized in the SPLC optimizations. The old cost function was a vestige from before 2014 when the shaped pupil apodizer was the entire coronagraph. The new cost function accounts for the approximate effects of the focal plane mask and Lyot stop on the off-axis transmission and can therefore achieve higher throughput without trading any other performance measure.

As shown in Figure 7, the achievable core throughput is over 0.8% higher with the new objective function than with the previous one when we also scan through different Lyot stop sizes and fix all other parameters. A third objective function was also tested. For a conventional Lyot coronagraph with an occulting spot FPM such as the APLC, the off-axis post-coronagraphic peak is equal to the transmission of the apodizer times the Lyot stop (at a field point sufficiently far from the occulter's edge). Maximizing the transmission of the shaped pupil times the Lyot stop does not improve throughput noticeably compared to the old objective function because the spatial filtering by the SPLC's FPM is still ignored.

When looking at Figure 8 at the on-axis and off-axis intensities at each plane for (a) the previous, January 2017 design (updated for primary mirror rollover) and (b) a new design, one can see how the new objective function is improving the throughput. In the previous design, the shaped pupil worked harder to make the Lyot plane dark within the annular opening of the Lyot stop from 26% to 88% of the pupil diameter. However, some of that effort was wasted because the off-axis light at the Lyot plane is virtually nonexistent at a radius of less than 45% of the D . Simply increasing the Lyot stop inner diameter actually decreased the throughput as shown in Figure 7 because the old cost function had no knowledge of the larger Lyot stop. When the post-coronagraphic peak is maximized instead as in Figure 8(b), the optimization now knows both to block on-axis starlight with the Lyot stop and to transmit off-axis light through it. We performed a grid search over FPM inner radius and Lyot stop inner and outer diameters to arrive at the improved design in Figure 8(b), which has an FPM opening from $5.2 - 20 \lambda_c/D$ and Lyot stop opening from 38%-87% of D . Compared to the January 2017 design, the new design provides a substantially smaller IWA ($6.8 \rightarrow 5.5 \lambda_c/D$) and a small throughput improvement ($5.20\% \rightarrow 5.50\%$).

We have begun investigating the potential benefits of this new, more appropriate cost function for the SPC-IFS design as well. Our early results show that the bowtie Lyot stop might need to be more open to achieve higher throughput with the new cost function.

6. OTHER POSSIBLE IMPROVEMENTS

The design improvements previously described in Sections 4 and 5 are helpful but not game-changing. They add little or no risk (or even reduce it) to the well-modeled and HCIT-tested SPLC architecture, but they provide only minor to medium gains in science yield. In this section, we present results from several ongoing investigations to

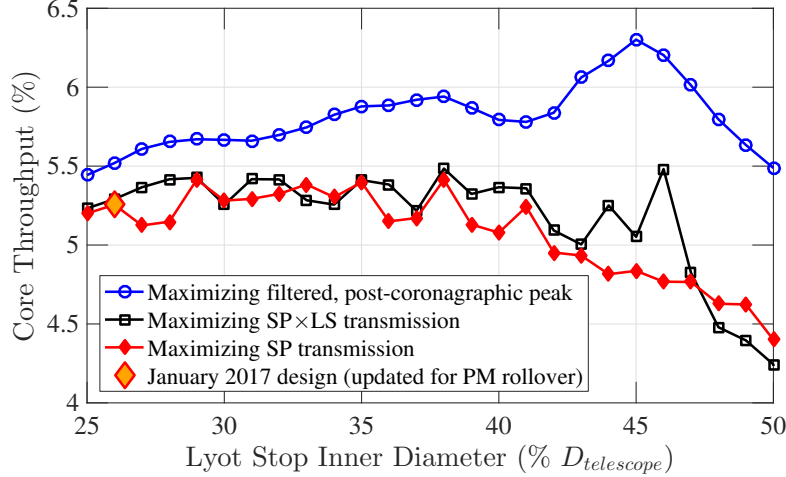


Figure 7. SPC-disk mode core throughput for different objective functions and Lyot stop inner diameters. All other constraints were the same: $6.5 - 20\lambda_c/D$ annular FPM opening, $88\% D$ Lyot stop outer diameter, and 8×10^{-10} raw contrast. Accounting for the FPM and Lyot stop in the cost function enable higher core throughput to be obtained. It is necessary to include spatial filtering of the shaped pupil to approximate off-axis transmission through the annular FPM; when only the shaped pupil times the Lyot stop is used as the cost function (which would be correct for an occulting spot FPM), the core throughput is not significantly better than when only the shaped pupil transmission is used as the cost function.

improve the science yield greatly (in particular by improving core throughput) with different choices of FPMs. These new FPMs would use the same manufacturing methods as the current SPLC and HLC FPMs, so they are allowed to be considered for the WFIRST CGI.

6.1 SPLC with Extended Bowtie FPM

The smallest departure from the SPLC's IFS mode is the SPLC-extended bowtie (SPLC-EBT). The only change from the original SPLC is that the bowtie FPM now has an outer radius larger than the desired dark hole in the final focal plane as shown in Figure 9. The original choice of having the dark hole match the bowtie shape was a logical starting point but is not required.

Allowing more light through the FPM enables more destructive interference in the dark hole and thus higher core throughput. Figure 10 shows this trend for the 2015-2016 SPLC-IFS design (without the primary mirror rollover blockage). The original design with the FPM outer radius and dark hole outer radius both at $9\lambda_c/D$ has less than 4% core throughput but lets less than 10^{-6} of all the starlight (that leaves the shaped pupil mask) through the Lyot stop. Increasing the FPM outer radius to $\geq 19\lambda_c/D$ gives over 6% core throughput but lets almost 10% of the starlight through the Lyot stop. Figure 10 (c) shows the intensities at the Lyot plane and final focal plane for a range of FPM outer radii.

The danger in allowing more light through the FPM and Lyot stop is that sensitivities worsen to T/T and other low-order Zernike aberrations. Figures 10 (a) and (b) show that there is no overlap between the FPM outer radii giving significantly higher throughput and those providing desirable aberration insensitivities. In our first tests including the direct T/T optimization from Section 4.2 in the SPLC-EBT optimizations, the throughput does not show the same improvement with increasing FPM outer radius. We have not yet tested whether this is from the bowtie Lyot stop limiting the throughput or from a possible incompatibility between higher throughput and lower T/T sensitivity. At the very least, we may adopt an FPM outer radius of $10 - 11\lambda_c/D$ to improve core throughput slightly without significantly degrading robustness to T/T or requiring a field stop for the final image.

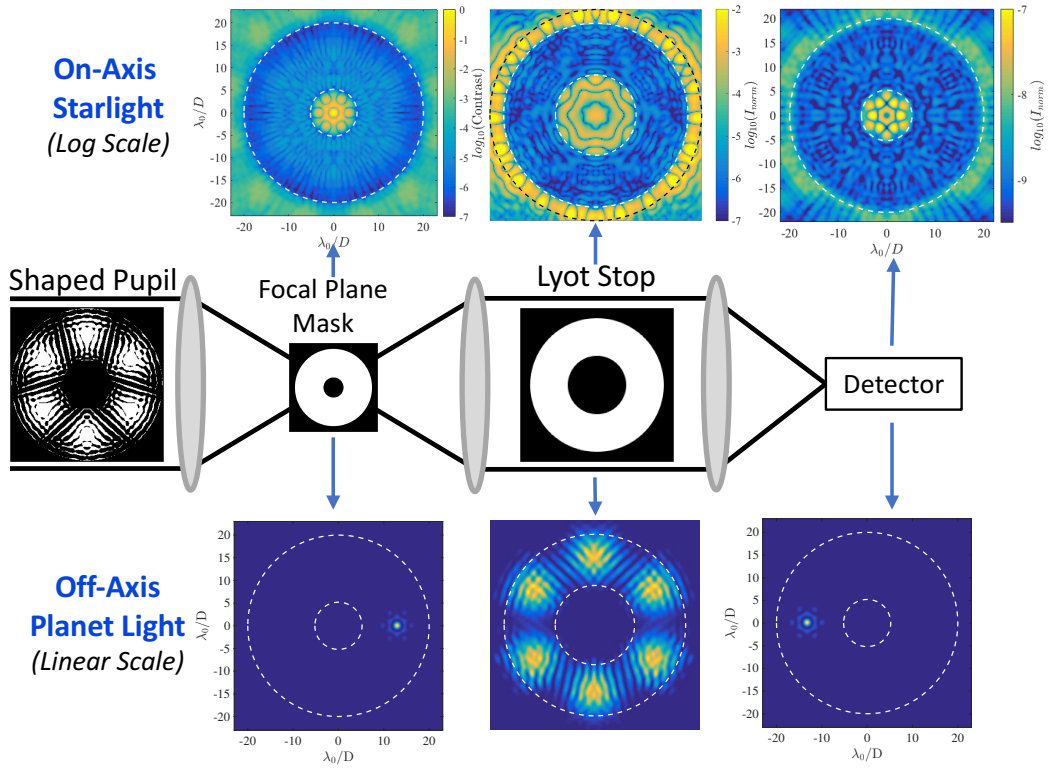
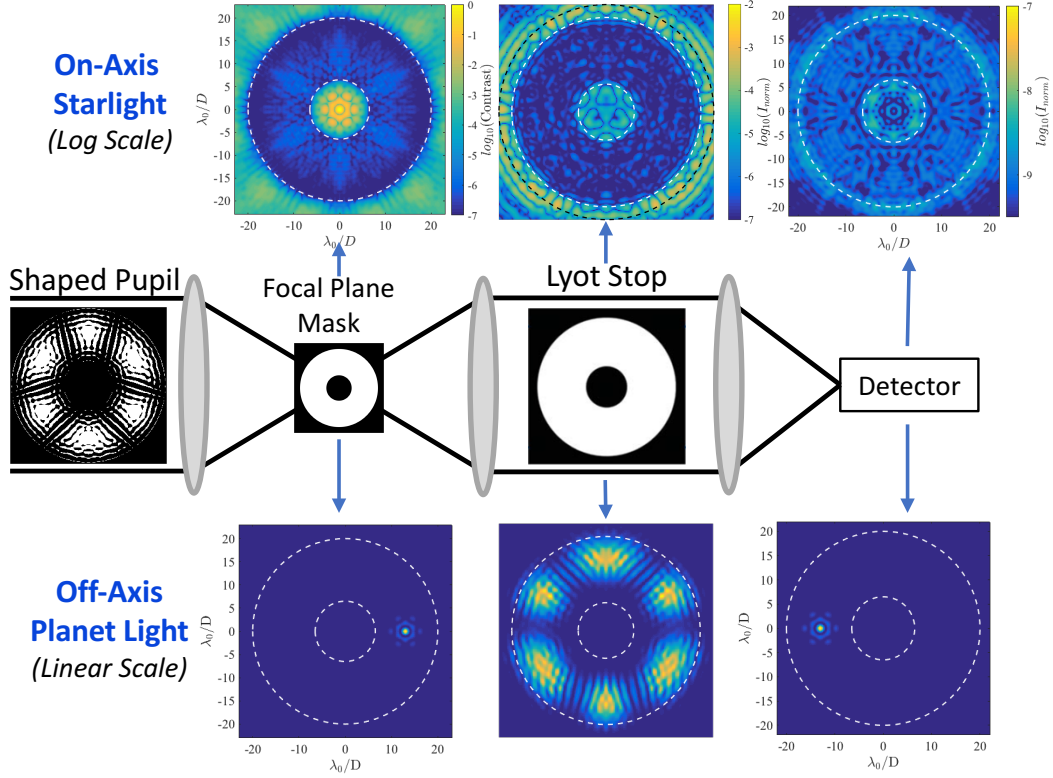


Figure 8. Diagrams of the on-axis and off-axis intensities at each pupil and focal plane for (a) the previous SPC-disk design and (b) the most recent SPC-disk design. The newer design increases throughput by offloading more of the stellar diffraction control from the shaped pupil to the Lyot stop. White dashed lines indicate the mask edges, and the black dashed lines indicate the pupil diameter in the Lyot plane.

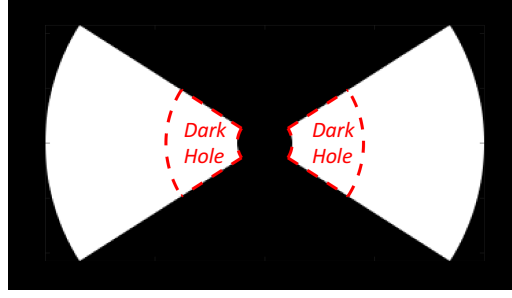


Figure 9. Extended bowtie (EBT) focal plane mask for use in the SPLC optimization. In this case, the dark hole in the second plane is not the same region of the bowtie FPM opening. Instead, the outer radius of the bowtie is extended past the outer radius of the dark hole. This enables more light to reach the Lyot plane for more destructive interference, but the sensitivities to low-order aberrations and Lyot stop misalignments increase.

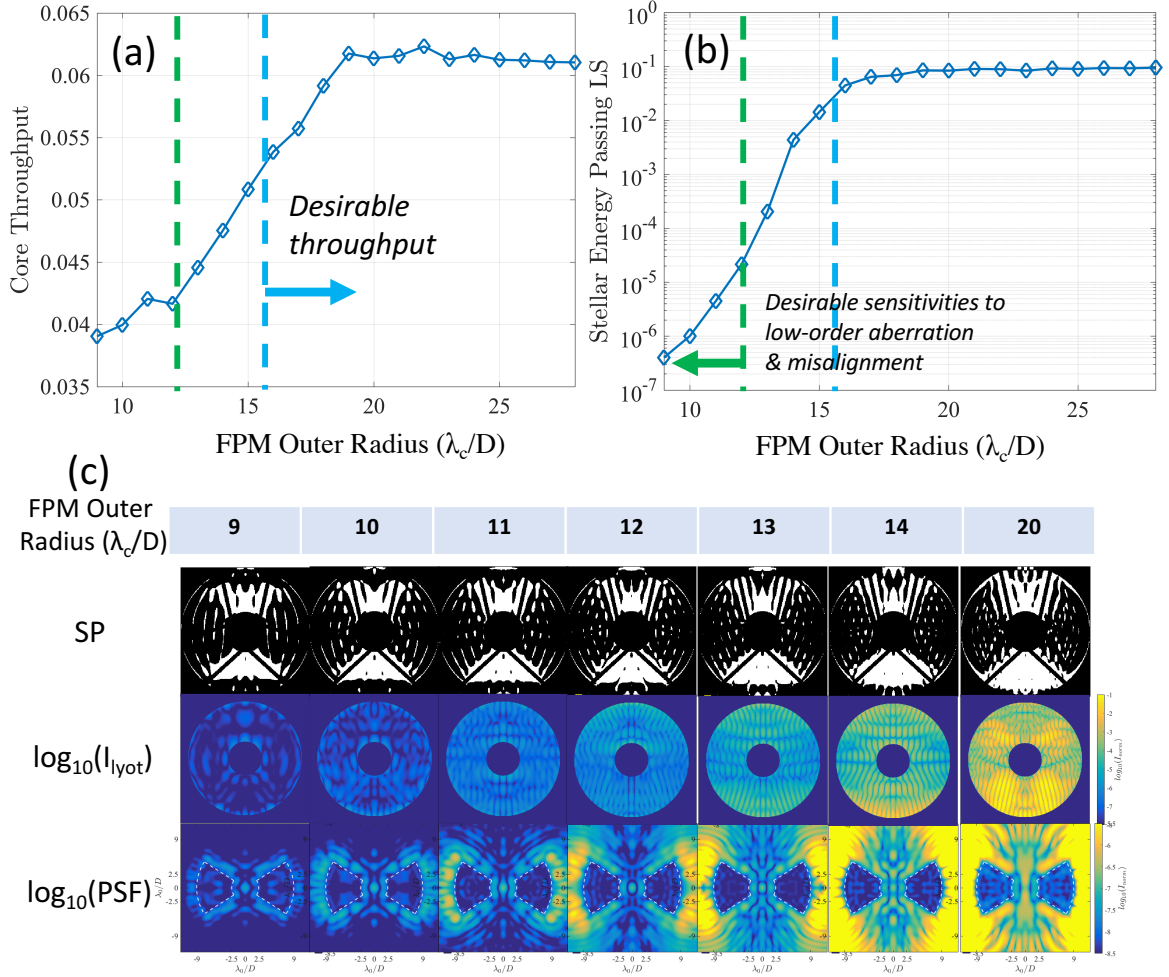


Figure 10. IFS-mode SPLC-EBT designs for increasing outer radii of the extended bowtie. (a) The core throughput increases for FPM outer radii up to $19 \lambda_c/D$, but (b) orders of magnitude more starlight passes through the Lyot stop in order to do so. (c) The on-axis intensities are shown for at the shaped pupil, Lyot plane, and final focal plane. The extra light in the Lyot stop opening degrades misalignment tolerances and adds the need for a downstream focal plane field stop.

6.2 APLC with $2 \times 65^\circ$ Dark Holes

The next study we performed for the spectroscopic CGI mode replaced the bowtie FPM with an opaque occulting spot. We refer to this as an APLC, but it uses a numerically optimized, binary-amplitude shaped pupil instead of the smooth, prolate apodization of a classical APLC. Just as with the SPLC-EBT, more light is allowed past the APLC's FPM and Lyot stop. The APLC tested here also had symmetric $2 \times 65^\circ$ dark holes to achieve a smaller IWA than possible with a full azimuthal field of view.

One APLC design, named SPC 20170123, was evaluated in the CGI flight model. This design has a $2.8\lambda_c/D$ occulting spot, $IWA=3.0\lambda_c/D$, $OWA=8.7\lambda_c/D$, annular Lyot stop open from 32%-86% of D , and a design raw contrast of 6×10^{-9} . The core throughput is significantly higher than for the SPLC at 7.2% (not accounting for the primary mirror rollover). The T/T sensitivity is better than for the SPLC, but the APLC cannot tolerate the polarization aberrations. Figure 11 shows simulated final PSFs from designs SPC 20170714 (the SPLC) and SPC 20170123 (the APLC) after performing wavefront correction on the full CGI flight model with all polarizations at the middle IFS bandpass. The large, ≈ 1 nm RMS astigmatism from the polarization aberrations heavily degrades the raw contrast at the APLC's IWA to almost 10^{-7} . Using an analyzer to block one polarization and one cross term would improve the contrast some (the other cross term would still remain) but cut the throughput in half. The SPLC would then have a higher effective throughput because it does not require polarization splitting. We have therefore stopped pursuing this type of design for the CGI.

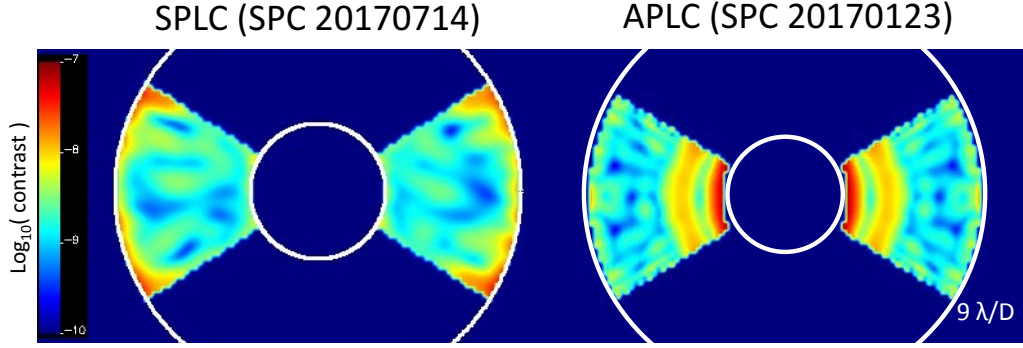


Figure 11. SPLC and APLC 18% broadband PSFs after wavefront control with the full WFIRST CGI flight model, including polarization aberrations. The APLC was evaluated at 800nm, and the SPLC was evaluated at 770nm, but the aberrations at each band are comparable. The SPLC is mostly immune to the polarization aberrations and still achieves 2×10^{-9} raw contrast. The APLC is much more sensitive to the astigmatism from the polarization aberrations, so it achieves only $\approx 10^{-7}$ raw contrast at the IWA.

6.3 APLC with an Occulting Bowtie FPM

We presume that the SPLC has better astigmatism (and other low-order Zernike) insensitivity than the APLC because the bowtie mask blocks most of the leakage around the core whereas the occulting spot does not. In an attempt to obtain the higher throughput of the APLC and the better low-order insensitivities of the SPLC, we invented the occulting bowtie (OBT) FPM. The OBT is similar to the previous bowtie mask but no longer blocks any light outside the outer mask radius. It is thus freestanding and would have to be laid on a substrate as the HLC occulter is. Figure 12 shows that the core throughput of the APLC-OBT generally increases with larger FPM outer radius, and the throughput can be twice as high for the APLC-OBT as for the equivalent APLC. OBT outer radii larger than $19 \lambda_c/D$ were not tested because the number of points in the FPM becomes prohibitively large.

Although the sensitivity to astigmatism (and therefore CGI polarization aberrations) improved somewhat, the APLC-OBT cannot tolerate expected levels of pointing jitter. We believe that the OBT having more edges causes the greater sensitivity to stellar speckles shearing along them from pointing errors. In future work, we will add the direct tip/tilt constraints from Section 4.2 into the APLC-OBT optimization. It is unclear how much throughput will be lost in trading for tip/tilt insensitivity.

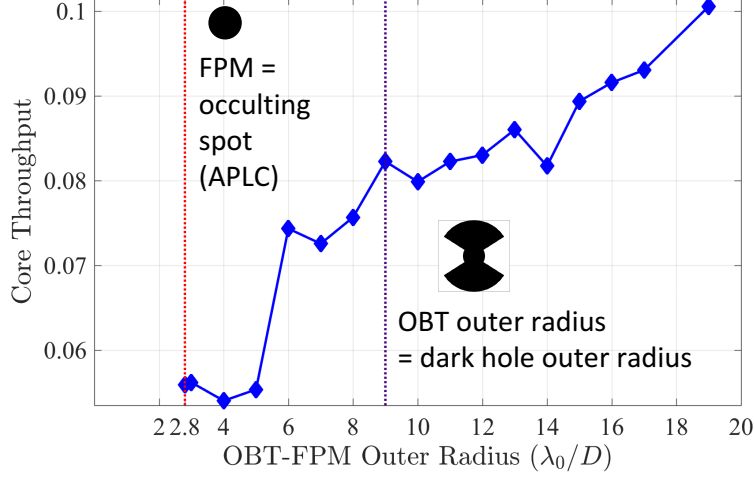


Figure 12. Core throughput of the APLC-OBT for an FPM inner radius of $2.8\lambda_c/D$ and different outer radii. The spectral bandwidth is 18%, and the average dark hole raw contrast is approximately 4×10^{-9} .

In addition to the low-order aberrations sensitivities, we need to model and address the alignment sensitivities of the Lyot stop for the APLC-OBT, particularly for the Lyot stop. Approximately 10%-20% of the starlight still passes through the Lyot stop—a million times more than for the SPLC. This means the APLC-OBT would be orders of magnitude more sensitive to clocking, translation, and/or magnification errors at the Lyot plane. The CGI’s HLC has similarly tight Lyot stop alignment tolerances but can adaptively overcome a static error with new deformable mirror commands. The DMs may also be able to mitigate the effects of small APLC Lyot stop misalignments.

6.4 APLC for Disk Science

The problematic T/T and other low-order Zernike sensitivities of the IFS-mode APLC and APLC-OBT arise from trying to obtain such a small IWA of $\approx 3 \lambda_c/D$. With a larger IWA and full 360° field of view, the APLC has sufficient low-order insensitivities and could be used for the observations of outer debris disks. In Figure 13, core throughput is plotted versus the FPM inner radius for disk science versions (with 360° field of view out to $20\lambda_c/D$) of the APLC and SPLC. The SPLCs have an annular Lyot stop opening from 45%-88% of D based on the best performance in Figure 7. The APLCs have an annular Lyot stop opening from 32%-86% of D ; this setting was not tuned due to time constraints, so there are likely APLC designs with better performance. Both the APLC and SPLC show a large falloff in throughput for inner spot radii smaller than $5.2\lambda_c/D$ and a mild increase for larger spots. This indicates that we may want to change the current SPLC-disk FPM inner radius from 6.5 to $5.2 \lambda_c/D$, as was shown in Figure 8(b). The core throughput for the APLC is consistently higher than for the SPLC with the same inner occulting spot size. However, the throughput gain shown here is not large enough, especially for an FPM inner radius of $5.2 \lambda_c/D$, to merit a switch to the APLC with its tighter Lyot stop alignment tolerances.

7. CONCLUSIONS AND FUTURE WORK

In this paper, we reported results for numerous methods to improve the optimization and performance of shaped pupil coronagraphs for the WFIRST CGI. Some of these changes improve the optimization process itself in terms of speed, numerical stability, and usability. We made modest improvements to the two baselined CGI SPLC modes for exoplanet spectroscopy and outer debris disk imaging. The SPLC for the IFS now has a more efficient Lyot stop providing higher throughput, better robustness to low-order aberrations, and a design pipeline to maximize the science yield. For the disk imaging SPLC, higher resolution (now 2000×2000) of the shaped pupil mask enables higher contrast, and a more appropriate cost function provides higher core throughput and a smaller inner working angle. In seeking higher core throughput, we investigated alternative designs with APLCs

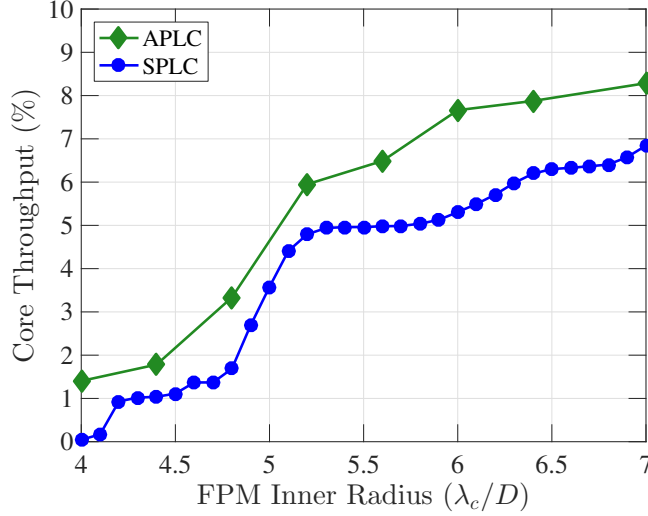


Figure 13. Core throughput dependence on focal plane mask (FPM) spot size for both APLC and SPLC disk science designs with 10% spectral bandwidth and $\approx 8 \times 10^{-10}$ raw contrast. The APLC has consistently higher throughput for any given mask radius at the expense of greater Lyot stop alignment tolerancing. The throughput for either type drops steeply for mask radii less than $5.2\lambda_c/D$. It may be worth trading some throughput to make the SPLC’s inner spot radius smaller than the current baselined size, down from $6.5\lambda_c/D$ to $5.2\lambda_c/D$. The APLC’s Lyot stop was not optimized due to insufficient time, so there are likely higher throughput APLC designs than the ones shown here.

for each the imaging and IFS modes. In each case, we found a tradeoff between better core throughput and better insensitivities to low-order Zernike aberrations and/or Lyot stop misalignment.

For our future coronagraph design work on the WFIRST CGI, we will continue our two-pronged strategy. In addition to fine tuning the SPLC architecture that we know works, we will investigate new methods for major performance gains, such as incorporating the deformable mirrors or a complex focal plane mask.

Acknowledgements

This work was performed at the Jet Propulsion Laboratory, California Institute of Technology, under a contract with the National Aeronautics and Space Administration. The authors acknowledge the support of WFIRST CGI team members at JPL and Princeton University, particularly Stuart Shaklan, Jeremy Kasdin, Jessica Gersh-Range, and Robert Vanderbei.

REFERENCES

- [1] Spergel, D., Gehrels, N., and et al., “Wide-Field InfrarRed Survey Telescope-Astrophysics Focused Telescope Assets WFIRST-AFTA 2015 Report,” *ArXiv e-prints*, 1503.03757 (March 2015).
- [2] for a Decadal Survey of Astronomy, C., [*New Worlds, New Horizons in Astronomy and Astrophysics*], Natl Academy Pr (2011).
- [3] Trauger, J., Moody, D., Krist, J., and Gordon, B., “Hybrid Lyot coronagraph for WFIRST-AFTA: coronagraph design and performance metrics,” *Journal of Astronomical Telescopes, Instruments, and Systems* **2**(1), 011013 (2016).
- [4] Zimmerman, N. T., Riggs, A. J. E., Jeremy Kasdin, N., Carlotti, A., and Vanderbei, R. J., “Shaped pupil Lyot coronagraphs: high-contrast solutions for restricted focal planes,” *Journal of Astronomical Telescopes, Instruments, and Systems* **2**(1), 011012 (2016).
- [5] Riggs, A. J. E., Zimmerman, N., Carlotti, A., Kasdin, N. J., and Vanderbei, R., “Shaped pupil design for future space telescopes,” in [*Proceedings of SPIE*], **9143**, 914325–914325–12 (2014).

- [6] Balasubramanian, K., White, V., Yee, K., Echternach, P., Muller, R., Dickie, M., Cady, E., Prada, C. M., Ryan, D., Poberezhskiy, I., Kern, B., Zhou, H., Krist, J., Nemati, B., Eldorado Riggs, A. J., Zimmerman, N. T., and Kasdin, N. J., “WFIRST-AFTA coronagraph shaped pupil masks: design, fabrication, and characterization,” *Journal of Astronomical Telescopes, Instruments, and Systems* **2**(1), 011005 (2015).
- [7] Balasubramanian, K. et al., “Systematic errors and defects in fabricated coronagraph masks and laboratory scale star-shade masks and their performance impact,” in [*Proceedings of SPIE*], **10400**, 12 (2017).
- [8] Cady, E., Prada, C. M., An, X., Balasubramanian, K., Diaz, R., Kasdin, N. J., Kern, B., Kuhnert, A., Nemati, B., Poberezhskiy, I., Riggs, A. J. E., Zimmer, R., and Zimmerman, N., “Demonstration of high contrast with an obscured aperture with the WFIRST-AFTA shaped pupil coronagraph,” *Journal of Astronomical Telescopes, Instruments, and Systems* **2**(1), 011004 (2015).
- [9] Cady, E. et al., “Shaped pupil coronagraphy for WFIRST: high-contrast broadband testbed demonstration,” in [*Proceedings of SPIE*], **10400**, 14 (2017).
- [10] Seo, B.-J., Gordon, B., Kern, B., Kuhnert, A., Moody, D., Muller, R., Poberezhskiy, I., Trauger, J., and Wilson, D., “Hybrid Lyot coronagraph for wide-field infrared survey telescope-astrophysics focused telescope assets: occulter fabrication and high contrast narrowband testbed demonstration,” *Journal of Astronomical Telescopes, Instruments, and Systems* **2**(1), 011019 (2016).
- [11] Seo, B.-J. et al., “Hybrid lyot coronagraph for WFIRST: high-contrast broadband testbed demonstration,” in [*Proceedings of SPIE*], **10400**, 15 (2017).
- [12] Krist, J., Nemati, B., and Mennesson, B., “Numerical modeling of the proposed WFIRST-AFTA coronagraphs and their predicted performances,” *Journal of Astronomical Telescopes, Instruments, and Systems* **2**(1), 011003 (2015).
- [13] Krist, J. E., Amiri, N., Gutt, G., Marchen, L., McGuire, J., Nemati, B., Saini, N., and Tang, H., “WFIRST coronagraph optical modeling,” in [*Proceedings of SPIE*], **10400**, 4 (2017).
- [14] Zhou, H. et al., “Wavefront control performance modeling with WFIRST shaped pupil coronagraph testbed,” in [*Proceedings of SPIE*], **10400**, 5 (2017).
- [15] Marx, D. S. et al., “Electric field conjugation in the presence of model uncertainty,” in [*Proceedings of SPIE*], **10400**, 23 (2017).
- [16] Sidick, E. et al., “Optimizing the regularization in broadband wavefront control algorithm for WFIRST coronagraph,” in [*Proceedings of SPIE*], **10400**, 74 (2017).
- [17] Kasdin, N. J., Vanderbei, R. J., Spergel, D. N., and Littman, M. G., “Extrasolar planet finding via optimal apodized-pupil and shaped-pupil coronagraphs,” *The Astrophysical Journal* **582**(2), 1147–1161 (2003).
- [18] Carlotti, A., Vanderbei, R., and Kasdin, N., “Optimal pupil apodizations of arbitrary apertures for high-contrast imaging,” *Optics Express* **19**(27), 26796–26809 (2011).
- [19] Vanderbei, R., “Fast Fourier optimization: Sparsity matters,” *Mathematical Programming Computation*, 1–17 (2012).
- [20] Soummer, R., Pueyo, L., Sivaramakrishnan, A., and Vanderbei, R., “Fast computation of Lyot-style coronagraph propagation,” *Optics Express* **15**(24), 15935–15951 (2007).
- [21] N’Diaye, M., Soummer, R., Pueyo, L., Carlotti, A., Stark, C. C., and Perrin, M. D., “Apodized pupil Lyot coronagraphs for arbitrary apertures. V. hybrid shaped pupil designs for imaging earth-like planets with future space observatories,” *The Astrophysical Journal* **818**(2), 163 (2016).
- [22] Krist, J., “Proper: an optical propagation library for IDL,” in [*Proc. of SPIE*], **6675**, 66750P (2007).
- [23] N’Diaye, M., Pueyo, L., Soummer, R., and Carlotti, A., “Apodized pupil lyot coronagraphs (aplc): development of designs with reduced iwa and robustness to low-order aberrations,” (2014).
- [24] Nemati, B. et al., “Sensitivity of the WFIRST coronagraph performance to key instrument parameters,” in [*Proceedings of SPIE*], **10400** (2017).
- [25] Zimmerman, N. T., Eldorado Riggs, A. J., Jeremy Kasdin, N., Carlotti, A., and Vanderbei, R. J., “Shaped pupil Lyot coronagraphs: high-contrast solutions for restricted focal planes,” *Journal of Astronomical Telescopes, Instruments, and Systems* **2**(1), 011012 (2016).